Fe(III) dihydroxybenzoquinone-based metal organic framework for sodium battery cathodes: Properties, charge-discharge kinetics and redox reaction mechanisms

Roman R. Kapaev [a], *, Ilgar Baghishov [b], Sergey V. Ryazantsev [c], Daniil Novichkov [d],
Igor A. Presniakov [d], Elena D. Orlova [e], Alexander Golubnichiy [e], Naman Katyal [b], Petr I. Matveev [d],
Graeme Henkelman [b], Keith J. Stevenson [d]

[a] Department of Chemistry and BINA – BIU Center for Nanotechnology and Advanced Materials, Bar-Ilan University, Ramat-Gan, 5290002, Israel
[b] Department of Chemistry, The University of Texas at Austin, Austin, TX, 78712-1224, USA
[c] Faculty of Materials Science, Shenzhen MSU-BIT University, Shenzhen, 517182, China
[d] Department of Chemistry, Lomonosov Moscow State University, Leninskie Gory 1/3, Moscow, 119991, Russia
[e] Center for Energy Science and Technology, Skolkovo Institute of Science and Technology, Bolshoy Boulevard 30 Bld. 1, Moscow, 121205, Russia

ABSTRACT

Sodium batteries are promising energy storage devices that could promote the transition to clean energy. For this purpose, it is desirable to develop safe cathode materials that can be easily produced from cheap and abundant elements. One of the attractive options is $Fe_2(dhbq)_3$, a metal-organic framework (MOF) that is synthesized from 2,5-dihydroxybenzoquinone (H_2dhbq) and Fe(III) salts. This work provides a comprehensive analysis of $Fe_2(dhbq)_3$, including its structure, properties, charge-discharge kinetics, and redox reaction mechanism in sodium batteries. Using a set of experimental and theoretical methods, we show that sodiation of $Fe_2(dhbq)_3$ in the potential range of 1.1–3.8 V vs. Na^+/Na is accompanied by a reversible two-electron reduction of dhbq ligands, while iron is only marginally involved and formally remains in $+3$ state. The material delivers a high specific capacity of up to ~180 mAh g^{-1}. Diffusion of Na^+ ions in $Na_xFe_2(dhbq)_3$ at low-to-moderate sodiation degrees (≥ 2.2 V vs. Na^+/Na) is so fast that it is kinetically indistinguishable from supercapacitance. Additionally, we show that $Fe_2(dhbq)_3$ can be synthesized by simply mixing solutions of H_2dhbq and salts of Fe(III) at room temperature, which makes its production especially simple and scalable.

1. Introduction

One of the most promising options for next-generation energy storage is sodium batteries [1,2]. Unlike Li-ion batteries, they can rely on abundant elements, which makes their large-scale production more sustainable [3,4]. To make sodium batteries cheaper and easier to make, it is desirable to develop cathode materials that could be synthesized from inexpensive chemicals in a straightforward and scalable way. Ideally, the synthesis should involve mixing of two solutions, followed by collecting and drying the resulting precipitate, which can be used for electrode production without further treatment. From this point of view, Prussian blue and its analogs ($Na_xM[Fe(CN)_6]_{(1-y)}*nH_2O$, M = Fe, Mn, Zn, etc.) are attractive candidates for cathode materials, since they can be synthesized simply by mixing hexacyanoferrates with transition metal salts in solution [5]. However, these compounds re-

lease toxic cyanides when heated up above 200 °C, which is a major safety concern [6]. Synthesis of other common cathode materials, such as transition metal oxides [7–12] and polyanionic structures [13–15], typically requires multistep procedures that involve energy-intensive high-temperature annealing.

Redox-active coordination polymers, including metal-organic frameworks (MOFs), have recently gained attention as energy storage materials [16–18]. Some redox-active MOFs have fast charge-discharge kinetics owing to their porous structures and high electron conductivity [19–23]. They can also combine high specific capacity and superior cycling stability [19–23]. Among the vast variety of building blocks that can be used for MOF synthesis, 2,5-dihydroxybenzoquinone (H_2dhbq) and Fe(III) salts are among the most appealing from a practical perspective. Dihydroxybenzoquinone is a cheap and stable redox-active ligand with a high specific capacity. Fe(III) compounds are extremely abun-

Note: Low-resolution images were used to create this PDF. The original images will be used in the final composition.

dant and stable in air. $Fe_2(dhbq)_3$ MOF has been reported to have high capacities and decent high-rate performance as a cathode material in Li- and Na-based cells [24,25].

However, the properties of $Fe_2(dhbq)_3$ have been poorly investigated, and its charge storage mechanism remains controversial. Cai et al. [24] reported that: (a) reduction of $Fe_2(dhbq)_3$ is partially irreversible for an unknown reason, (b) Fe(II) and $dhbq^{2.2-}$ coexist in a partially reduced state, and (c) Fe(II) and Fe(III) coexist in a fully reduced state at 1.5 V vs. Li^+/Li. These points are in contradiction with other studies of the Fe(III)-dhbq framework, where it is reported that $dhbq^{3-}$ anions coexist with Fe(III) [26,27], and that Fe(III) is not reduced to Fe (II) even by sodium naphthalenide [26], which has an oxidation potential of ~0.5 V vs. Li^+/Li [28]. Gupta et al. [25] reported that energy of the X-ray absorption Fe K-edge decreases upon lithiation, but does not reach the value characteristic for Fe(II)-dhbq. Surprisingly, X-ray near edge absorption spectra (XANES) of the reduced and reoxidized $Fe_2(dhbq)_3$ were reported to be almost identical. The charge storage mechanism of $Fe_2(dhbq)_3$ in batteries was explored using only lithium-based systems, while no mechanistic studies reported for sodium-based cells.

Previous studies have a few major limitations. First, all measurements were performed *ex situ*, so limited information about the redox processes could be obtained. Second, the experimental data was not supported by computational approaches, which left some ambiguity in the interpretation of the data. Here we present a comprehensive study of $Fe_2(dhbq)_3$ properties, its charge-discharge kinetics and redox reaction mechanism in sodium-ion batteries. We use a set of complementary *ex situ* and *operando* techniques, as well as density functional theory (DFT) calculations to gain a detailed understanding of the $Fe_2(dhbq)_3$ structure and its evolution upon sodiation. Additionally, we show that $Fe_2(dhbq)_3$ can be obtained simply by mixing solutions of H_2dhbq and salts of Fe(III) at room temperature, which makes the synthesis simple and scalable.

2. Experimental section

2.1. Fe-dhbq MOF synthesis

In a typical synthesis, a solution of $Fe(NO_3)_3*9H_2O$ (14 mmol, 4.656 g) in 50 mL of ethanol was added under continuous stirring to a solution of 2,5-dihydroxybenzoquinone (21 mmol, 2.942 g) in 450 mL of ethanol. The precipitate was collected by centrifugation and washed with 200 mL of ethanol. The product was dried in a vacuum oven at 150 °C.

2.1.1. Caution!

Reaction between iron (III) nitrate and dihydroxybenzoquinone leads to formation of HNO_3 as a byproduct. In higher concentrations, HNO_3 reacts with alcohols (including ethanol) forming aggressive and explosive substances [29,30]. To eliminate any risk of incidents when scaling up the synthesis, it is advised to replace iron (III) nitrate with another salt, such as iron (III) chloride. According to powder X-ray diffraction (Fig. S1), using $FeCl_3$ instead of $Fe(NO_3)_3*9H_2O$ leads to the same product.

2.2. Electrode preparation

To prepare the electrodes for the electrochemical studies and *operando* Raman spectroscopy, $Fe_2(dhbq)_3$ (80 % wt., 480 mg), Super P carbon black (10 % wt., 60 mg) and poly(vinylidene difluoride) (10 % wt., 60 mg) dissolved in *N*-methylpyrrolidone (2.0 mL) were thoroughly mixed to form a homogeneous slurry. The slurry was deposited onto a carbon-coated Al foil using tape-casting (the slurry thickness was 150 μm for the galvanostatic experiments and 70 μm for the cyclic voltammetry and *operando* Raman spectroscopy studies), dried in air at

70 °C and then vacuum-dried at 110 °C overnight. The electrodes were calendered at room temperature and subjected to additional vacuum-drying at 110 °C for 5–10 h. The loading of Fe-dhbq was 2.0 mg cm^{-2} for the galvanostatic experiments and 0.9 mg cm^{-2} for the cyclic voltammetry and *operando* Raman spectroscopy studies.

To prepare the electrodes for the *ex situ* studies, $Fe_2(dhbq)_3$ (70 % wt., 700 mg), Super P carbon black (15 % wt., 150 mg) and poly(vinylidene difluoride) (15 % wt., 150 mg) were thoroughly mixed in presence of *N*-methyl pyrrolidone (~0.6–0.8 mL) to form a plasticine-like substance, which was then calendered at room temperature with a thickness of ~400–500 μm, oven-dried at 70 °C for 30 min, then calendered at 80–85 °C with a thickness of 300 μm. The resulting free-standing electrodes were vacuum-dried at 110 °C overnight. The loading of $Fe_2(dhbq)_3$ was ~20 mg cm^{-2}.

2.3. Cell assembling

All cells used for this study were assembled in an Ar-filled glovebox with oxygen level below 10 ppm. Sodium metal was used for the counter-electrodes, glass fiber filters were used as the separators. 1.5 M $NaPF_6$ solution in dry diglyme was used as the electrolyte for the *operando* Raman measurements, 1.5 M $NaPF_6$ solution in dry 1,2-dimethoxyethane was used for all other experiments. For the *ex situ* studies, additional layers of polyolefin-based Celgard separators were placed between the cathodes and the glass fiber separators to avoid sticking of the glass fiber to the electrodes. For the electrochemical studies, CR2032-type coin cells were assembled. The electrolyte volume per cell was 75–80 μL. For the *ex situ* studies, disassemblable cells (ECC-Ref, EL-Cell) were assembled in a two-electrode configuration. The electrolyte volume per cell was 100 μL. For the *operando* Raman spectroscopy studies, a cell with an optically transparent glass window (ECC-Opto-Std, EL-Cell) was assembled in a two-electrode configuration. Cathodes were cut into strips (~1 mm width, ~1 cm length), and strips were placed in direct contact with the glass window with the active material facing the window.

2.4. Galvanostatic cycling and electrochemical sodiation

The galvanostatic experiments were performed using Neware BTS-4000 or BioLogic VMP-3 stations at room temperature. The potential range for the cycling was 1.1–3.8 V vs. Na^+/Na. The cycling was started with discharge, *i.e.*, decrease of the cell voltage. If not stated otherwise, the current densities and capacities were calculated per mass of Fe-dhbq.

2.5. Cyclic voltammetry

The cyclic voltammograms were measured at room temperature with BioLogic VMP-3 in the potential range of 1.1–3.8 V vs. Na^+/Na. Before doing the primary experiments, the cells were pre-conditioned by running five cycles at a scan rate of 0.1 mV s^{-1}.

2.6. FTIR spectroscopy

FTIR spectra were measured with Bruker ALPHA II in ATR mode (diamond crystal). The spectrometer was placed in a nitrogen-filled glovebox with oxygen level below 10 ppm and water level below 0.1 ppm. The spectrum of $Fe_2(dhbq)_3$ powder was measured immediately after it was vacuum-dried at 150 °C.

2.7. Raman spectroscopy

The Raman spectra were measured with a Thermo Scientific DXRxi Raman imaging microscope equipped with a green laser (λ = 532 nm).

The laser power was set to 0.5 mW to avoid burning the samples. All Raman spectra were baseline-corrected with Bruker OPUS software.

For the *operando* measurements, the cell was placed inside the spectrometer and connected to a BioLogic SP-150 potentiostat. The Raman spectra were collected at room temperature during a CV scan in the potential range of 1.1–3.8 V vs. Na^+/Na with a scan rate of 0.05 mV s^{-1}. Single scans were measured every 6 min (18 mV per scan) with a range of Raman shifts between 50 and 2200 cm^{-1}.

2.8. X-ray diffraction (XRD)

The XRD pattern of the pristine material was measured with Bruker D8 ADVANCE operating with CuK_α radiation (λ = 1.5406 Å), 2θ range was 5–60°, resolution was 0.01°. XRD patterns of free-standing electrodes were measured in transmission mode using Huber Guinier Camera 670 operating with $CoK_{\alpha1}$ radiation (λ = 1.78892 Å), 2θ range was 4–100°, resolution was 0.005°.

To measure the sodiated material, a free-standing electrode was discharged at room temperature to 1.1 V vs. Na^+/Na, current density was 10 mA g^{-1}. The cell was disassembled in an Ar-filled glovebox, the electrode was washed with ~4 mL of 1,2-dimethoxyethane and dried in the glovebox at room temperature. The electrode was placed onto a Mylar film in a sample holder for the Huber Guinier Camera 670, and the holder was sealed with a Kapton tape to prevent decomposition in air during the measurements. The sample was then taken out from the glovebox. The measurements were carried out directly after the Kapton-sealed electrodes were removed from the glovebox. Single scans were measured in the 2θ range of 4–100° each 10 min to monitor possible changes caused by oxidation. The measurements continued overnight. The scans that were measured before changes in the XRD patterns started to occur were then averaged.

2.9. Scanning electron microscopy

SEM images were acquired using a Thermo Fisher Helios G4 PFIB microscope with an acceleration voltage of 2 kV.

2.10. Transmission electron microscopy

Transmission electron microscopy (TEM) and high-angle annular dark-field scanning transmission electron microscopy (HAADF-STEM) images were acquired with a Thermo Fisher Titan Themis Z transmission electron microscope equipped with a Super-X system for energy-dispersive X-ray spectroscopy. The acceleration voltage was set to 200 kV. TEM samples were prepared in air by crushing the powder with an agate mortar and pestle and depositing the powder onto a carbon film supported by a copper grid without solvent to avoid interactions between solvent and the studied material.

2.11. Elemental analysis

Contents of carbon and hydrogen were determined using express gravimetric analysis with Elementar vario MICRO cube. SEM EDX measurements were performed using a Thermo Fisher Quattro S ESEM microscope; the sample was placed onto a silver-based SEM holder to avoid interference with the signals from the sample. Compositional EDX maps obtained in STEM mode were acquired with Thermo Fisher Titan Themis Z, magnification was 270,000x, pixel size was ~0.7 nm.

2.12. Specific surface area analysis

Nitrogen adsorption-desorption isotherms were measured at 77 K using a Quantachrome NOVAtouch surface analyzer. The sample was degassed *in vacuo* at 200 °C for 1.5 h before the measurements. BET surface area was calculated using BETSI software [31].

2.13. Pellet preparation and conductivity measurements

A cylindrical pellet (d = 10 mm) was prepared via cold pressing of the pristine powder with an applied pressure of 5 tons for 30 s. Before the conductivity measurements were made, the top and bottom of the pellet were coated with gold (~100 nm) using magnetron sputtering with Quorum Q150R ES. The pellet was placed in a symmetrical cell between two copper disks. Conductivity was measured in air at room temperature using direct-current (DC) polarization with a BioLogic VMP3 instrument. The voltage was changed in 10 mV steps between −0.4 and 0.4 V in forward and backward directions, starting from 0 V.

2.14. Differential scanning calorimetry (DSC) analysis

DSC measurements were performed using a Netzsch DSC 214 Polyma instrument under nitrogen with a heating rate of 10 K min^{-1}.

2.15. Thermogravimetric analysis-mass spectrometry (TGA-MS)

TGA-MS measurements were carried out using a Netzsch TG-DSC STA-449F3 instrument combined with a Netzsch QMS 403 D Aëolos mass spectrometer. The powders were heated at a 10 K min^{-1} rate from room temperature to 600 °C under an argon flow.

2.16. Mössbauer spectroscopy

^{57}Fe Mössbauer spectra were measured for pristine Fe_2 $(dhbq)_3$ and a free-standing electrode discharged in galvanostatic mode at 10 mA g^{-1} to 1.1 V. The cell was disassembled in an Ar-filled glovebox, and the sodiated electrode was sealed in a polypropylene holder using PTFE and Kapton tapes to avoid oxidation in air. The measurements were carried out in transmission geometry with a 1500 MBq γ-source of ^{57}Co(Rh), which was mounted on a conventional constant acceleration drive. Isomer shifts refer to α-iron at room temperature. The spectra were analyzed using the SpectrRelax software [32] to obtain a model fitting and reconstruction of distribution of hyperfine parameters.

2.17. X-ray absorption spectroscopy

Fe K-edge X-ray absorption spectra were measured for free-standing electrodes in pristine and discharged states as well as for reference compounds – FeS and $FeCl_3$ for Fe(II) and Fe(III), respectively. Discharge was performed in galvanostatic mode at 10 mA g^{-1} to 1.1 V, the discharged cell was disassembled in an argon-filled glovebox, and the sodiated electrode was sealed in Kapton films. The spectra were acquired using a spectrometer in the Department of Radiochemistry, Moscow State University [33]. An X-ray tube with an Ag anode, with a power of 1.5 kW, was used as the radiation source. The X-ray tube, crystal monochromator, and silicon drift detector (Amptek) were placed in a 0.5 m diameter Rowland circle. Measurements were conducted in the energy range of 7050–7550 eV with a 1 eV step and a constant measurement time of 5 s per energy point. A Ge [620] crystal monochromator was utilized, where the scanned Bragg angle varied from 79.42 to 66.62°. To prevent sample damage by a polychromatic beam, samples were positioned in front of the detector, where they were exposed only to monochromatic radiation. The beam size was 5*5 mm. The data were acquired in transmission mode. For each sample, 8 scans were collected and merged into one dataset. The obtained data were processed using the *Larch* software package [34], which includes the *feff8* code [35] for calculating phases and amplitudes of scattering paths. EXAFS data were Fourier-transformed within 2.0–9.0 $Å^{-1}$ k-range (Kaiser-Bessel window, dk = 3.0, k-weighting 2.0).

2.18. Computations

Density functional theory (DFT) simulations were performed using the Vienna ab initio simulation package (VASP) [36] unless specified otherwise. The electronic structure was optimized with the Perdew–Burke–Ernzerhof functional [37] within the generalized gradient approximation. All calculations were performed considering spin-polarization. Core electrons were treated using the projector augmented-wave method. The Kohn–Sham wave functions representing valence electrons were expanded in a plane wave basis set with an energy cutoff of 300 eV, and a single Γ-point was employed for the integration of reciprocal space. While additional k-points were tested, their inclusion did not yield a significant change in the energy. Force convergence tolerance for ionic optimization and energy convergence tolerance for the electronic optimizations were set at 0.01 eV Å^{-1} and 10^{-7} eV, respectively. The initial MOF structure was obtained from a recently published paper [25], forming the basis for subsequent investigations.

To characterize the voltage profile, first, the DFT energy of the structure was calculated at various sodiation levels ranging from 1 to 6 Na atoms per Fe$_2$(dhbq)$_3$. The convex hull was constructed to assess the stability of the configurations by setting pristine MOF and fully sodiated MOF as references using the following equation:

$$Energy(x) = E_{Na_xFe_2(dhbq)_3} - \left(1 - \frac{x}{6}\right) E_{Fe_2(dhbq)_3} - \frac{x}{6} E_{Na_6Fe_2(dhbq)_3}$$

Here, x is the number of Na per formula unit of the electrode material and $E_{Na_xFe_2(dhbq)_3}$ is the DFT energy of the MOF sodiated with x Na atoms per Fe$_2$(dhbq)$_3$

Voltage profiles were constructed from energy points on the convex hull when the number of Na atoms increases from x_1 to x_2:

$$Voltage = -\frac{\left(E_{Na_{x2}Fe_2(dhbq)_3} - E_{Na_{x_1}Fe_2(dhbq)_3}\right)}{x_2 - x_1}$$

Raman spectra of pristine and sodiated structures were simulated using methodology explained elsewhere [38,39]. For FTIR simulation, the process described in Ref. [40] was followed where Born effective charges were determined using density functional perturbation theory in VASP.

Multiple scattering calculations of extended X-ray absorption fine structure (EXAFS) spectra for pristine and sodiated structures were simulated by employing an approach similar to previous work [41,42]. Fe EXAFS spectra were derived by selecting 2000 snapshots from a DFT molecular dynamics trajectory at 300 K using a time step of 1 ps, averaging the signals from each Fe atom.

The diffraction pattern of the simulated structure and their atomic positions in this work were generated using the VESTA Package [43]. Bader charge analysis was performed on core and valence electron charge densities from VASP [44].

3. Results and discussion

3.1. Synthesis and characterization

Fe$_2$(dhbq)$_3$ was synthesized by mixing solutions of 2,5-dihydroxybenzoquinone and a Fe(III) salt in ethanol at room temperature, where the product precipitates instantly. The process requires no reflux, long reaction time or inert atmosphere, which appeared in previously published synthetic procedures [24,25].

Powder XRD pattern of Fe$_2$(dhbq)$_3$ (Fig. 1a) is in agreement with the literature data [24,25]. The compound crystallizes in space group *Fddd*, forming a three-dimensional porous framework with intertwined layers where each Fe is chelated by three ligands in a slightly distorted octahedral environment [25]. No major changes are observed after DFT geometry optimization of this crystal structure (Table S1). FTIR spectrum, which was measured in N$_2$ atmosphere for the thoroughly dried sample, also matches the literature data (Fig. 1b) [24,25]. The vibrational spectra of Fe$_2$(dhbq)$_3$ are distinct from free dihydroxybenzoquinone H$_2$dhbq (Fig. 1b and c). In particular, the O–H stretching band (~3300 cm^{-1}) is absent, and C=O/C=C stretching modes of H$_2$dhbq (~1600–1670 cm^{-1}) are shifted to lower frequencies, which indicates that the ligands are chelated by iron [26,45]. According to EDX and CH-analysis, the elemental composition of the material is close to that calculated for Fe$_2$(C$_6$H$_2$O$_4$)$_3$; no elements except for C, O and Fe are observed in the EDX (Fig. 1d). ^{57}Fe Mössbauer spectrum of Fe$_2$(dhbq)$_3$ (Fig. 1e) is characteristic for a high-spin Fe(III) compound, in accordance with the previous reports [24,25].

X-ray absorption Fe K-edge energy also characteristic for Fe(III) (Fig. 1f). The R-space plot of the EXAFS data (Fig. 1g) features two principal maxima in the $1.0 < R < 2.7$ Å, corresponding to the first and the second coordination spheres of iron atoms. The EXAFS data in this range can be fitted well using a simple model of symmetrical environment of absorbing Fe atoms (six equivalent O atoms as the first shell plus six equivalent C atoms as the second shell), yielding average Fe–O and Fe–C distances of 2.02 ± 0.015 and 2.84 ± 0.04 Å, respectively, which (taking uncertainty into account) agrees well with the structural data reported earlier. The details of the EXAFS data fitting are given in Table S2. Our EXAFS cannot reveal slight asymmetry of the FeO$_6$ octahedra because more complex models for local Fe environment would demand a number of fitting parameters exceeding the number of independent parameters, rendering any such fit statistically unreliable. For the same reason, we limited the data range for fitting – many scattering paths are involved at R > 2.7 Å, each contributing additional variables for the fitting. The EXAFS simulation performed using molecular dynamics with DFT shows reasonable agreement with experimental data (Fig. S2). Overall, the measurements confirm the structure of Fe$_2$(dhbq)$_3$.

According to electron microscopy, the particle size of the material ranges from ~20 to ~80 nm, with a median value of 45 nm (Fig. 1h–j). TEM EDX mapping with a sub-nanometer resolution shows a homogeneous distribution of the elements (Fig. 1k). The MOF has a high BET surface area of 789 m^2 g^{-1}, and the nitrogen adsorption profile reveals a sharp gas uptake at low pressures, which is characteristic of microporous materials (Fig. 1l). Electrical conductivity of the pelletized powder is 3.6*10^{-7} S cm^{-1} at room temperature (Fig. 1m). The conductive nature of Fe$_2$(dhbq)$_3$ is an indicator of π-d conjugation between the ligand and metal nodes [46].

To study the thermal stability of Fe$_2$(dhbq)$_3$, we combined DSC and TGA-MS techniques. The DSC profile reveals a broad endothermic peak at ~110 °C upon heating (Fig. 1n). According to TGA-MS (Fig. 1o), it corresponds to desorption of water, which is adsorbed by Fe$_2$(dhbq)$_3$ when it is exposed to ambient air [24]. Decomposition of the material takes place above 300 °C, with H$_2$O and CO$_2$ as the main volatile decomposition products (Fig. 1o). These results demonstrate the high thermal stability of Fe$_2$(dhbq)$_3$.

3.2. Electrochemical properties

Fe$_2$(dhbq)$_3$ was tested in sodium cells in the potential range of 1.1–3.8 V vs. Na$^+$/Na, the electrolyte was 1 M NaPF$_6$ solution in dimethoxyethane. The working electrodes, which were prepared in ambient air, contained 80 % wt. of the MOF and only 10 % wt. of carbon black as a conductive filler, which is lower than typically used for organic-based sodium battery cathodes (30–50 % wt.) [47–52]. The as-prepared electrodes were vacuum-dried at 150 °C before assembling the cells to remove the absorbed water. Details are available in the Experimental sections 2.2–2.5.

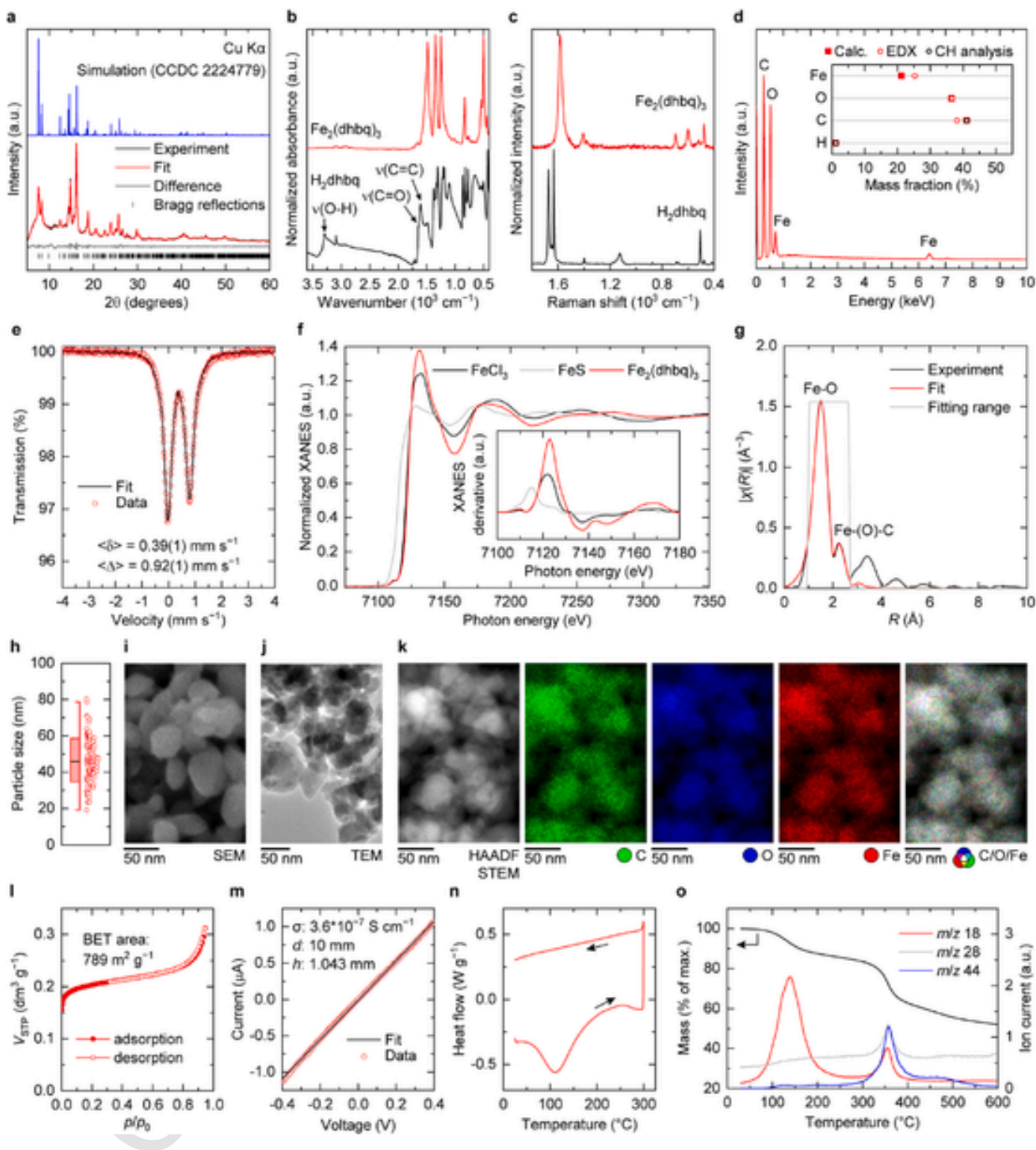**Fig. 1.** Characterization of $Fe_2(dhbq)_3$: (a) XRD pattern vs. a Le Bail fit and simulated pattern for the previously reported crystal structure [25]; (b) FTIR and (c) Raman spectra of H_2dhbq and $Fe_2(dhbq)_3$; (d) EDX spectrum and elemental composition according to EDX and CH-analysis; (e) ^{57}Fe Mössbauer spectrum; (f) Fe K-edge XANES and its derivative compared to reference compounds; (g) EXAFS in R-space and k-space; (h) distribution of the particle size estimated from SEM images; (i) SEM image; (j) TEM image; (k) HAADF-STEM image and EDX elemental mapping; (l) low-temperature N_2 adsorption-desorption isotherms; (m) DC polarization data for the pelletized powder; (n) DSC profile; (o) TGA-MS profiles.

$Fe_2(dhbq)_3$ shows a high reversible capacity of up to $\sim$180 mAh g^{-1} and exhibits decent high-rate performance (Fig. 2a, Fig. S5). The MOF is redox active in the potential range from $\sim$1.5 to $\sim$3.5 V vs. Na^+/Na, with an average discharge potential of >2.2 V (Fig. 2b). The energy-power output of $Fe_2(dhbq)_3$, although not record-high, is competitive with state-of-the art cathode materials for sodium batteries, especially at the electrode level (see Table S3, Figs. S3 and S4). Furthermore, the material exhibits superior cycling performance for up to a thousand cycles (Fig. 2c and d). Another attractive feature of $Fe_2(dhbq)_3$ is the low irreversible capacity loss in the first cycle, which is only 4 % (Fig. S5), while for many advanced organic-based materials it is typically $\geq$20 % [47,53–58]. It indicates that reduction/oxidation of $Fe_2(dhbq)_3$ is reversible.

Interestingly, the average discharge potential of $Fe_2(dhbq)_3$ increases at higher currents (Fig. 2b). This is untypical since higher currents impose higher overpotentials, which should lead to the decrease

of the discharge voltage [59–61]. This phenomenon is due to the different kinetics of the material upon reduction at higher and lower sodiation degrees. It can be seen from Fig. 2a that the discharge profiles at $\geq$2.2 V change only slightly, while the capacity at lower potentials decreases significantly. Therefore, contribution of the higher-voltage region to the total capacity increases at higher current rates. This result shows that $Fe_2(dhbq)_3$ has fast sodiation kinetics at $\geq$2.2 V vs. Na^+/Na. The fast kinetics is also confirmed by cyclic voltammetry, revealing that there is a nearly linear dependence of the cathodic current on the potential scan rate at $\geq$2.2 V vs. Na^+/Na (Fig. S6). These results indicate that diffusion of Na^+ ions in $Na_xFe_2(dhbq)_3$ at low-to-moderate sodiation degrees is so fast that it is kinetically indistinguishable from supercapacitance [62,63]. Such behavior should be associated with the porous structure of $Fe_2(dhbq)_3$, which enables rapid movement of the ions within the material [25].

DFT calculations indicate that $Fe_2(dhbq)_3$ can accept up to two Na^+/electrons per dhbq unit, which implies that the fully sodiated material has a formula $Na_6Fe_2(dhbq)_3$. The simulated voltage profile (Fig. 2e) is in fair agreement with the experimental discharge curve at 20 mA g^{-1}. The convex energy hull (Fig. 2f) shows that $Na_xFe_2(dhbq)_3$ structures are the most stable at $x = 1.33, 2.0, 2.67, 4.0,$ and 6.0. The theoretical capacity is 305.8 mAh g^{-1} if calculated per $Fe_2(dhbq)_3$ mass unit and 242.2 mAh g^{-1} if calculated per $Na_6Fe_2(dhbq)_3$ mass unit. The experimental specific capacity is smaller due to several reasons. Firstly, there is kinetic hindrance during sodiation/desodiation at lower potentials (<2.2 V vs. Na^+/Na). Secondly, $Fe_2(dhbq)_3$ inevitably absorbs water during the electrode preparation in ambient air, and the mass of water is not excluded when the experimental capacity is calculated. Other factors, such as material degradation and slight dissolution in the electrolyte, can also play a minor role. The practical capacity of $Fe_2(dhbq)_3$ is subject to further improvement, e.g., via optimizing the composition or preparation procedure of the electrodes.

3.3. Charge storage mechanism

Operando Raman spectroscopy shows that sodiation of $Fe_2(dhbq)_3$ is reversible (Fig. 3a), which agrees with low initial irreversible capacity loss (Fig. S5); the similarity of *ex situ* FTIR spectra of pristine and recharged electrodes further confirms the reversibility (Fig. 3d). Upon desodiation, the material goes through the same phases as upon sodiation, which is indicated by symmetrical changes of the spectra (Fig. 3a).

Remarkably, the Raman spectrum of the fully sodiated $Fe_2(dhbq)_3$ shares a similar pattern to fully sodiated $[Ni(C_6H_2(NH_2)_4)]_n$ (NiBTA), which is a nickel coordination polymer derived from 1,2,4,5-benzenetetramine (Fig. 3c) [64]. It was previously shown that NiBTA undergoes two-electron reduction of the ligands, while nickel is only marginally involved in the redox reactions [64]. Since the structures of dhbq and $C_6H_2(NH)_4$ moieties are alike (the only difference is that dhbq has oxygen atoms instead of NH groups); the similarity of the Raman spectra indicates that two-electron reduction of dhbq ligands takes place in the case of $Fe_2(dhbq)_3$. Raman peaks at $\sim$1200–1600 cm^{-1} correspond to bond length alternation modes of the ligands, signals at $\sim$500–650 cm^{-1} can be assigned to Fe–O (Ni–N) stretching modes, and the peak at $\sim$750–760 cm^{-1} corresponds to a breathing mode of the ligands that becomes active only in the reduced state [64]. For $Na_xFe_2(dhbq)_3$, signals at $\sim$1000–1200 cm^{-1}, which stay almost intact upon charging-discharging, do not belong to the MOF (see Fig. 1c) and likely originate from the electrolyte in the sodium cell. The spectra also have a minor constant contribution from the carbon black additive, which has a characteristic G-band at $\sim$1600 cm^{-1} and a D-band at $\sim$1350 cm^{-1} [65].

The simulated vibrational spectra cannot be used to reliably determine the charge storage mechanisms of $Fe_2(dhbq)_3$ since the peak intensities of the vibrational spectra strongly depend on the structure
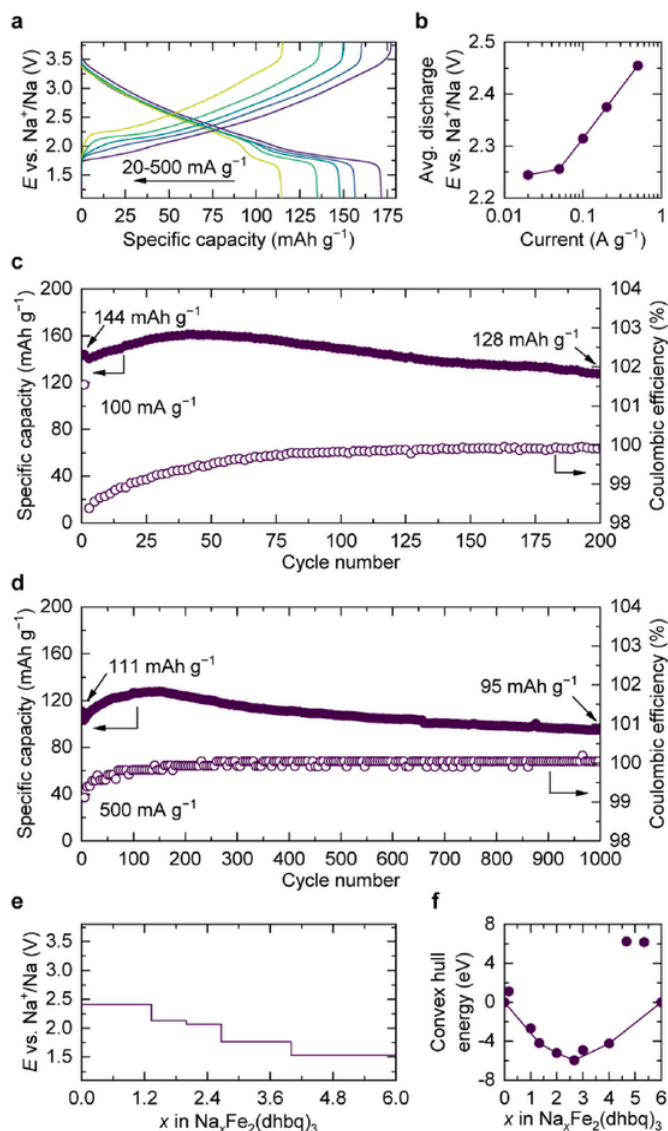

Fig. 2. Electrochemical properties of Fe_2 (dhbq)$_3$ in sodium cells: (a) charge-discharge profiles at 20, 50, 100, 200 and 500 mA g^{-1}; (b) average discharge potential at different specific currents; (c, d) cycling stability at 100 and 500 mA g^{-1}, respectively; (e) simulated discharge profile; (f) calculated formation energies for the $Na_xFe_2(dhbq)_3$ system to predict possible ground state structures at intermediate sodiation levels.
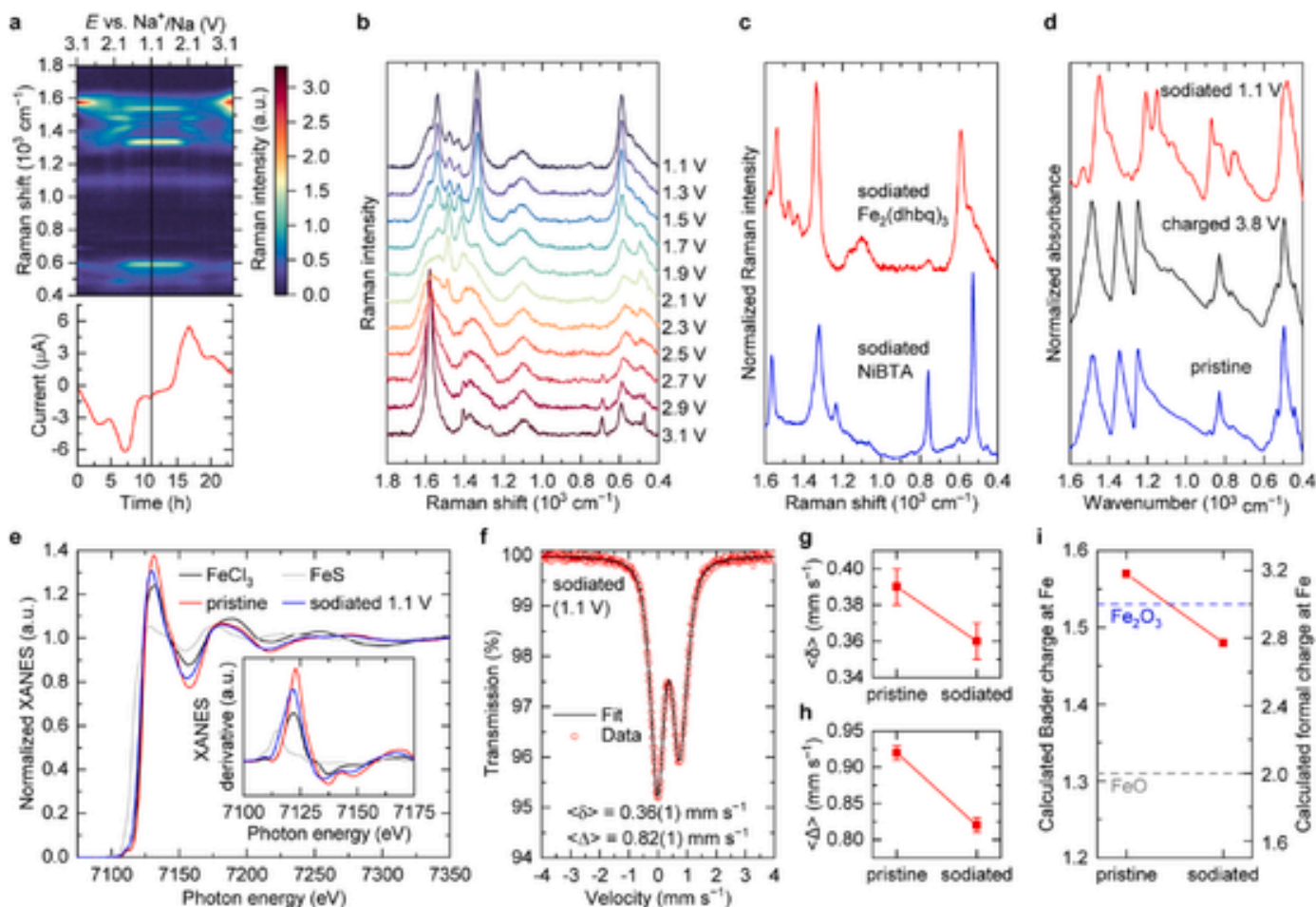
Fig. 3. Mechanistic studies of $Fe_2(dhbq)_3$: (a) *operando* Raman intensity map plotted with current vs. time (vs. potential) profile; (b) Raman spectra of at various potentials; (c) Raman spectrum of fully sodiated $Fe_2(dhbq)_3$ compared to the simulated spectrum of $Na_6Fe_2(dhbq)_3$ and experimental spectrum for Na_2NiBTA; (d) *ex situ* FTIR spectra of the electrodes in various states of charge compared to the simulated spectrum of $Na_6Fe_2(dhbq)_3$; (e) XANES of pristine and discharged electrodes compared to reference compounds; (f) ^{57}Fe Mössbauer spectrum of the fully sodiated electrode; (g) mean isomer shift and (h) mean quadrupole splitting for pristine and fully sodiated electrodes; (i) calculated Bader and formal charges of iron in $Fe_2(dhbq)_3$ and $Na_6Fe_2(dhbq)_3$ compared to Fe_2O_3 and FeO.

symmetry, which is different for the experimental and DFT-optimized structures (space group is *P1* for the DFT-optimized structure of $Fe_2(dhbq)_3$ while it is *Fddd* for the experimental one, see Table S1). Moreover, it is challenging to predict the exact position of sodium ions within the lattice because of the computational complexity of sodiated structures. As a result, the simulated vibrational spectra deviate substantially from the experimental measurements (Fig. S7). A possible reason for the discrepancy between theory and experiment might be the presence of small impurities or absorbed species, such as residual solvent in the material.

According to XRD, the MOF remains crystalline in the fully sodiated state (Fig. S8). However, reliable determination of the sodiated crystal structure from the powder XRD data is an issue, again because it is challenging to locate the sodium ions within the lattice using DFT. We suggest that further studies employing single-crystal XRD or electron diffraction are needed.

XANES shows that Fe K-edge energy shifts to slightly lower values upon sodiation (Fig. 3e), which indicates that electron density in the vicinity of iron increases. However, the edge energy for the fully sodiated $Fe_2(dhbq)_3$ is still higher than for iron (II) sulfide or Fe(II)-dhbq MOF [25]. Mössbauer spectrum of the sodiated $Fe_2(dhbq)_3$ is still typical for high-spin Fe(III) (Fig. 3f), and only minor changes of isomer shift and quadrupole splitting parameters are observed (Fig. 3g and h). DFT

computations are in accordance with these data, showing that the Bader charges at iron are only slightly lower for $Na_6Fe_2(dhbq)_3$ compared to $Fe_2(dhbq)_3$ (Fig. 3i). A calculated differential charge distribution map (Fig. S9) shows that the charge gained upon reduction of $Fe_2(dhbq)_3$ is delocalized over the entire MOF structure. Experimental and simulated EXAFS of the fully sodiated MOF are in good agreement, both showing negligible increase (≤ 0.01 Å) of Fe–O and Fe–(O)–C distances compared to pristine $Fe_2(dhbq)_3$ (Fig. S10). Overall, it can be concluded that the formal oxidation state of iron remains $+3$ and reduction of $Fe_2(dhbq)_3$ is ligand-centered.

4. Conclusion

$Fe_2(dhbq)_3$ can be easily synthesized from cheap and abundant reagents and has high thermal stability. Since this MOF is electrically conductive, it exhibits decent performance in electrodes with low content of conductive fillers. $Fe_2(dhbq)_3$ demonstrates fast sodium ion diffusion rates at ≥ 2.2 V vs. Na^+/Na, which makes it kinetically indistinguishable from supercapacitive processes. In the potential range of 1.1–3.8 V vs. Na^+/Na, reduction of $Fe_2(dhbq)_3$ is ligand-based, while Fe units are only marginally involved in the redox chemistry, formally staying as Fe(III) in the fully sodiated form $Na_6Fe_2(dhbq)_3$. The reduction is reversible, which is indicated by vibrational spec-

troscopy and low irreversible capacity losses at the first cycle. To summarize, $Fe_2(dhbq)_3$ is an attractive cathode material for sodium batteries.

Notes

The authors declare no competing financial interest.

CRediT authorship contribution statement

Roman R. Kapaev: Writing – review & editing, Writing – original draft, Visualization, Methodology, Investigation, Formal analysis, Conceptualization. **Ilgar Baghishov:** Writing – review & editing, Visualization, Methodology, Investigation, Formal analysis. **Sergey V. Ryazantsev:** Writing – review & editing, Validation, Methodology, Formal analysis, Data curation. **Daniil Novichkov:** Writing – review & editing, Methodology, Investigation, Formal analysis. **Igor A. Presniakov:** Writing – review & editing, Methodology, Investigation, Formal analysis. **Elena D. Orlova:** Writing – review & editing, Methodology, Investigation, Formal analysis. **Alexander Golubnichiy:** Writing – review & editing, Methodology, Investigation, Formal analysis. **Naman Katyal:** Writing – review & editing, Validation, Supervision, Methodology. **Petr I. Matveev:** Supervision, Project administration, Funding acquisition. **Graeme Henkelman:** Writing – review & editing, Supervision, Project administration, Funding acquisition. **Keith J. Stevenson:** Writing – review & editing, Supervision, Project administration, Funding acquisition.

Declaration of competing interest

The authors declare that they have no known competing financial interests or personal relationships that could have appeared to influence the work reported in this paper.

Data availability

Data will be made available on request.

Appendix A. Supplementary data

Supplementary data to this article can be found online at https://doi.org/10.1016/j.jpowsour.2024.234679.

ABBREVIATIONS

ATR	attenuated total reflectance
DC	direct current
DFT	density functional theory
DSC	differential scanning calorimetry
EDX	energy-dispersive X-ray spectroscopy
EXAFS	Extended X-ray absorption fine structure
FTIR	Fourier-transform infrared spectroscopy
HAADF-STEM	high-angle annular dark-field scanning transmission electron microscopy
MS	mass-spectrometry
PTFE	polytetrafluoroethylene
SEM	scanning electron microscopy
TEM	transmission electron microscopy
TGA	thermogravimetric analysis
XANES	X-ray absorption near edge spectrum
XRD	X-ray diffraction

References

[1] N. Yabuuchi, K. Kubota, M. Dahbi, S. Komaba, Research development on sodium-ion batteries, Chem. Rev. 114 (2014) 11636–11682, https://doi.org/10.1021/cr500192f.

[2] C. Delmas, Sodium and sodium-ion batteries: 50 Years of research, Adv. Energy Mater. 8 (2018) 1703137, https://doi.org/10.1002/aenm.201703137.

[3] Q. Liu, Z. Hu, M. Chen, C. Zou, H. Jin, S. Wang, S.-L. Chou, Y. Liu, S.-X. Dou, The cathode choice for commercialization of sodium-ion batteries: layered transition metal oxides versus prussian blue analogs, Adv. Funct. Mater. 30 (2020) 1909530, https://doi.org/10.1002/adfm.201909530.

[4] C. Vaalma, D. Buchholz, M. Weil, S. Passerini, A cost and resource analysis of sodium-ion batteries, Nat. Rev. Mater. 3 (2018) 18013, https://doi.org/10.1038/natrevmats.2018.13.

[5] J. Peng, W. Zhang, Q. Liu, J. Wang, S. Chou, H. Liu, S. Dou, Prussian blue analogues for sodium-ion batteries: past, present, and future, Adv. Mater. 34 (2022) 2108384, https://doi.org/10.1002/adma.202108384.

[6] Z. Li, M. Dadsetan, J. Gao, S. Zhang, L. Cai, A. Naseri, M.E. Jimenez-Castaneda, T. Filley, J.T. Miller, M.J. Thomson, V.G. Pol, Revealing the thermal safety of prussian blue cathode for safer nonaqueous batteries, Adv. Energy Mater. 11 (2021) 2101764, https://doi.org/10.1002/aenm.202101764.

[7] T. Li, M. Lu, Y. Zhang, X. Xiang, S. Liu, C. Chen, Structural evolution and redox chemistry of robust ternary layered oxide cathode for sodium-ion batteries, J. Alloys Compd. 978 (2024) 173459, https://doi.org/10.1016/j.jallcom.2024.173459.

[8] S. Liu, J. Wan, M. Ou, W. Zhang, M. Chang, F. Cheng, Y. Xu, S. Sun, C. Luo, K. Yang, C. Fang, J. Han, Regulating Na occupation in P2-type layered oxide cathode for all-climate sodium-ion batteries, Adv. Energy Mater. 13 (2023) 2203521, https://doi.org/10.1002/aenm.202203521.

[9] B. Wang, J. Ma, K. Wang, D. Wang, G. Xu, X. Wang, Z. Hu, C.-W. Pao, J.-L. Chen, L. Du, X. Du, G. Cui, High-Entropy phase stabilization engineering enables high-

performance layered cathode for sodium-ion batteries, Adv. Energy Mater. (2024) 2401090, https://doi.org/10.1002/aenm.202401090.

[10] Z. Wang, L. Fang, X. Fu, S. Zhang, H. Kong, H. Chen, F. Fu, A Ni/Co-free high-entropy layered cathode with suppressed phase transition and near-zero strain for high-voltage sodium-ion batteries, Chem. Eng. J. 480 (2024) 148130, https://doi.org/10.1016/j.cej.2023.148130.

[11] H. Lu, S. Chu, J. Tian, Q. Wang, C. Sheng, C. Cheng, R. Liu, A.M. D'Angelo, W.K. Pang, L. Zhang, H. Zhou, S. Guo, Ultra-high-energy density in layered sodium-ion battery cathodes through balancing lattice-oxygen activity and reversibility, Adv. Funct. Mater. 34 (2024) 2305470, https://doi.org/10.1002/adfm.202305470.

[12] B. Chen, Y. Xin, Y. Wang, X. Ding, C. Jiang, F. Wu, H. Gao, Modulating the oxygen redox activity of an ultra-high capacity P3 type cathode for sodium-ion batteries via beryllium introduced, Energy Storage Mater. 67 (2024) 103252, https://doi.org/10.1016/j.ensm.2024.103252.

[13] C. Liu, K. Chen, H. Xiong, A. Zhao, H. Zhang, Q. Li, X. Ai, H. Yang, Y. Fang, Y. Cao, A novel Na₈Fe₅(SO₄)₉@rGO cathode material with high rate capability and ultra-long lifespan for low-cost sodium-ion batteries, eScience 4 (2024) 100186, https://doi.org/10.1016/j.esci.2023.100186.

[14] X. Li, J. Zhang, Y. Zhang, B. Zhang, H. Liu, Q. Xu, Y. Xia, A facile Ball-Milling preparation strategy of Nitrogen-Doped carbon coated Na₄Fe₃(PO₄)₂P₂O₇ Nano-Flakes with superior sodium ion storage performance, Chem. Eng. Sci. 260 (2022) 117951, https://doi.org/10.1016/j.ces.2022.117951.

[15] X. Lin, X. Ren, L. Cong, Y. Liu, X. Xiang, Reversible multi-electron reaction mechanism of sodium vanadium/manganese phosphate cathode for enhanced Na-storage capability, Chemelectrochem 9 (2022) e202200669, https://doi.org/10.1002/celc.202200669.

[16] J. Liu, M. Zheng, S. Wu, L. Zhang, Design strategies for coordination polymers as electrodes and electrolytes in rechargeable lithium batteries, Coord. Chem. Rev. 483 (2023) 215084, https://doi.org/10.1016/j.ccr.2023.215084.

[17] Z. Liang, C. Qu, W. Guo, R. Zou, Q. Xu, Pristine metal–organic frameworks and their composites for energy storage and conversion, Adv. Mater. 30 (2018) 1702891, https://doi.org/10.1002/adma.201702891.

[18] H.B. Wu, X.W. Lou, Metal-organic frameworks and their derived materials for electrochemical energy storage and conversion: promises and challenges, Sci. Adv. 3 (2017) eaap9252, https://doi.org/10.1126/sciadv.aap9252.

[19] J. Park, M. Lee, D. Feng, Z. Huang, A.C. Hinckley, A. Yakovenko, X. Zou, Y. Cui, Z. Bao, Stabilization of hexaaminobenzene in a 2D conductive metal–organic framework for high power sodium storage, J. Am. Chem. Soc. 140 (2018) 10315–10323, https://doi.org/10.1021/jacs.8b06020.

[20] S. Dong, L. Wu, M. Xue, Z. Li, D. Xiao, C. Xu, L. Shen, X. Zhang, Conductive metal–organic framework for high energy sodium-ion hybrid capacitors, ACS Appl. Energy Mater. 4 (2021) 1568–1574, https://doi.org/10.1021/acsaem.0c02758.

[21] K.W. Nam, S.S. Park, R. dos Reis, V.P. Dravid, H. Kim, C.A. Mirkin, J.F. Stoddart, Conductive 2D metal-organic framework for high-performance cathodes in aqueous rechargeable zinc batteries, Nat. Commun. 10 (2019) 4948, https://doi.org/10.1038/s41467-019-12857-4.

[22] S. Gu, Z. Bai, S. Majumder, B. Huang, G. Chen, Conductive metal–organic framework with redox metal center as cathode for high rate performance lithium ion battery, J. Power Sources 429 (2019) 22–29, https://doi.org/10.1016/j.jpowsour.2019.04.087.

[23] B. Zhu, D. Wen, Z. Liang, R. Zou, Conductive metal-organic frameworks for electrochemical energy conversion and storage, Coord. Chem. Rev. 446 (2021) 214119, https://doi.org/10.1016/j.ccr.2021.214119.

[24] T. Cai, Z. Hu, Y. Gao, G. Li, Z. Song, A rationally designed iron–dihydroxybenzoquinone metal–organic framework as practical cathode material for rechargeable batteries, Energy Storage Mater. 50 (2022) 426–434, https://doi.org/10.1016/j.ensm.2022.05.040.

[25] S. Gupta, H. Tanaka, K. Fuku, N. Iguchi, H. Iguchi, R. Sakamoto, H. Kobayashi, Y. Gambe, I. Honma, Y. Hirai, S. Hayami, S. Takaishi, Quinoid-based three-dimensional metal–organic framework Fe₂(dhbq)₃: porosity, electrical conductivity, and solid-state redox properties, Inorg. Chem. 62 (2023) 6306–6313, https://doi.org/10.1021/acs.inorgchem.2c04313.

[26] L.E. Darago, M.L. Aubrey, C.J. Yu, M.I. Gonzalez, J.R. Long, Electronic conductivity, ferrimagnetic ordering, and reductive insertion mediated by organic mixed-valence in a ferric semiquinoid metal–organic framework, J. Am. Chem. Soc. 137 (2015) 15703–15711, https://doi.org/10.1021/jacs.5b10385.

[27] J.A. DeGayner, I.-R. Jeon, L. Sun, M. Dincă, T.D. Harris, 2D conductive iron-quinoid magnets ordering up to Tc = 105 K via heterogenous redox chemistry, J. Am. Chem. Soc. 139 (2017) 4175–4184, https://doi.org/10.1021/jacs.7b00705.

[28] J. Jang, I. Kang, J. Choi, H. Jeong, K.-W. Yi, J. Hong, M. Lee, Molecularly tailored lithium–arene complex enables chemical prelithiation of high-capacity lithium-ion battery anodes, Angew. Chem. Int. Ed. 59 (2020) 14473–14480, https://doi.org/10.1002/anie.202002411.

[29] F.H. Hedlund, M.F. Nielsen, S.H. Mikkelsen, E.K. Kragh, Violent explosion after inadvertent mixing of nitric acid and isopropanol – review 15 years later finds basic accident data corrupted, no evidence of broad learning, Saf. Sci. 70 (2014) 255–261, https://doi.org/10.1016/j.ssci.2014.06.010.

[30] E. Camera, G. Modena, B. Zotti, On the behaviour of nitrate esters in acid solution. III. Oxidation of ethanol by nitric acid in sulphuric acid, Propellants Explos. Pyrotech. 8 (1983) 70–73, https://doi.org/10.1002/prep.830080303.

[31] J.W.M. Osterrieth, J. Rampersad, D. Madden, N. Rampal, L. Skoric, B. Connolly, M.D. Allendorf, V. Stavila, J.L. Snider, R. Ameloot, J. Marreiros, C. Ania, D. Azevedo, E. Vilarrasa-Garcia, B.F. Santos, X.-H. Bu, Z. Chang, H. Bunzen, N.R. Champness, S.L. Griffin, B. Chen, R.-B. Lin, B. Coasne, S. Cohen, J.C. Moreton, Y.J. Colón, L. Chen, R. Clowes, F.-X. Coudert, Y. Cui, B. Hou, D.M. D'Alessandro, P.W. Doheny, M. Dincă, C. Sun, C. Doonan, M.T. Huxley, J.D. Evans, P. Falcaro, R. Ricco, O. Farha, K.B. Idrees, T. Islamoglu, P. Feng, H. Yang, R.S. Forgan, D. Bara, S. Furukawa, E. Sanchez, J. Gascon, S. Telalović, S.K. Ghosh, S. Mukherjee, M.R. Hill, M.M. Sadiq, P. Horcajada, P. Salcedo-Abraira, K. Kaneko, R. Kukobat, J. Kenvin, S. Keskin, S. Kitagawa, K.-i. Otake, R.P. Lively, S.J.A. DeWitt, P. Llewellyn, B.V. Lotsch, S.T. Emmerling, A.M. Pütz, C. Martí-Gastaldo, N.M. Padial, J. García-Martínez, N. Linares, D. Maspoch, J.A. Suárez del Pino, P. Moghadam, R. Oktavian, R.E. Morris, P.S. Wheatley, J. Navarro, C. Petit, D. Danaci, M.J. Rosseinsky, A.P. Katsoulidis, M. Schröder, X. Han, S. Yang, C. Serre, G. Mouchaham, D.S. Sholl, R. Thyagarajan, D. Siderius, R.Q. Snurr, R.B. Goncalves, S. Telfer, S.J. Lee, V.P. Ting, J.L. Rowlandson, T. Uemura, T. Iiyuka, M.A. van der Veen, D. Rega, V. Van Speybroeck, S.M.J. Rogge, A. Lamaire, K.S. Walton, L.W. Bingel, S. Wuttke, J. Andreo, O. Yaghi, B. Zhang, C.T. Yavuz, T.S. Nguyen, F. Zamora, C. Montoro, H. Zhou, A. Kirchon, D. Fairen-Jimenez, How reproducible are surface areas calculated from the BET equation? Adv. Mater. 34 (2022) 2201502, https://doi.org/10.1002/adma.202201502.

[32] M.E. Matsnev, V.S. Rusakov, Study of spatial spin-modulated structures by Mössbauer spectroscopy using SpectrRelax, AIP Conf. Proc. 1622 (2014) 40–49, https://doi.org/10.1063/1.4898609.

[33] D. Novichkov, A. Trigub, E. Gerber, I. Nevolin, A. Romanchuk, P. Matveev, S. Kalmykov, Laboratory-based X-ray spectrometer for actinide science, J. Synchrotron Radiat. 30 (2023) 1114–1126, https://doi.org/10.1107/S1600577523006926.

[34] M. Newville, Larch: an analysis package for XAFS and related spectroscopies, J. Phys. Conf. 430 (2013) 012007, https://doi.org/10.1088/1742-6596/430/1/012007.

[35] A.L. Ankudinov, B. Ravel, J.J. Rehr, S.D. Conradson, Real-space multiple-scattering calculation and interpretation of x-ray-absorption near-edge structure, Phys. Rev. B 58 (1998) 7565–7576, https://doi.org/10.1103/PhysRevB.58.7565.

[36] G. Kresse, J. Furthmüller, Efficient iterative schemes for ab initio total-energy calculations using a plane-wave basis set, Phys. Rev. B 54 (1996) 11169–11186, https://doi.org/10.1103/PhysRevB.54.11169.

[37] J.P. Perdew, K. Burke, M. Ernzerhof, Generalized gradient approximation made simple, Phys. Rev. Lett. 77 (1996) 3865–3868, https://doi.org/10.1103/PhysRevLett.77.3865.

[38] A. Llordés, Y. Wang, A. Fernandez-Martinez, P. Xiao, T. Lee, A. Poulain, O. Zandi, C.A. Saez Cabezas, G. Henkelman, D.J. Milliron, Linear topology in amorphous metal oxide electrochromic networks obtained via low-temperature solution processing, Nat. Mater. 15 (2016) 1267–1273, https://doi.org/10.1038/nmat4734.

[39] A. Fonari, S. Stauffer, GitHub - Raman-sc/VASP: Python program to evaluate off-resonance Raman activity using VASP code as the backend, https://github.com/raman-sc/VASP. (Accessed 17 December 2023).

[40] D. Karhánek, GitHub - dakarhanek/VASP-infrared-intensities: a simple BASH script for extraction of infared intensities from DFPT calculation output by VASP code, https://github.com/dakarhanek/VASP-infrared-intensities. (Accessed 17 December 2023).

[41] D.F. Yancey, S.T. Chill, L. Zhang, A.I. Frenkel, G. Henkelman, R.M. Crooks, A theoretical and experimental examination of systematic ligand-induced disorder in Au dendrimer-encapsulated nanoparticles, Chem. Sci. 4 (2013) 2912–2921, https://doi.org/10.1039/C3SC50614B.

[42] S.I. Zabinsky, J.J. Rehr, A. Ankudinov, R.C. Albers, M.J. Eller, Multiple-scattering calculations of x-ray-absorption spectra, Phys. Rev. B 52 (1995) 2995–3009, https://doi.org/10.1103/PhysRevB.52.2995.

[43] K. Momma, F. Izumi, VESTA 3 for three-dimensional visualization of crystal, volumetric and morphology data, J. Appl. Crystallogr. 44 (2011) 1272–1276, https://doi.org/10.1107/S0021889811038970.

[44] W. Tang, E. Sanville, G. Henkelman, A grid-based Bader analysis algorithm without lattice bias, J. Phys. Condens. Matter 21 (2009) 084204, https://doi.org/10.1088/0953-8984/21/8/084204.

[45] M. Habeeb, H.A. Al-Wakil, A. El-Dissouky, N.M. Refat, Vibrational spectroscopic studies of hydrogen–bonded complexes between 2,5-dihydroxy-P-benzoquinone and amines, Spectroscopy 15 (2001) 721903, https://doi.org/10.1155/2001/721903.

[46] L.S. Xie, G. Skorupskii, M. Dincă, Electrically conductive metal–organic frameworks, Chem. Rev. 120 (2020) 8536–8580, https://doi.org/10.1021/acs.chemrev.9b00766.

[47] M. Tang, S. Zhu, Z. Liu, C. Jiang, Y. Wu, H. Li, B. Wang, E. Wang, J. Ma, C. Wang, Tailoring π-conjugated systems: from π-π stacking to high-rate-performance organic cathodes, Chem 4 (2018) 2600–2614, https://doi.org/10.1016/j.chempr.2018.08.014.

[48] M. Lee, J. Hong, J. Lopez, Y. Sun, D. Feng, K. Lim, W.C. Chueh, M.F. Toney, Y. Cui, Z. Bao, High-performance sodium–organic battery by realizing four-sodium storage in disodium rhodizonate, Nat. Energy 2 (2017) 861–868, https://doi.org/10.1038/s41560-017-0014-y.

[49] R. Shi, L. Liu, Y. Lu, Y. Li, S. Zheng, Z. Yan, K. Zhang, J. Chen, In situ polymerized conjugated poly(pyrene-4,5,9,10-tetraone)/carbon nanotubes composites for high-performance cathode of sodium batteries, Adv. Energy Mater. 11 (2021) 2002917, https://doi.org/10.1002/aenm.202002917.

[50] C. Wang, R. Chu, Z. Guan, D. Ullah, H. Song, Y. Zhang, C. Yu, L. Zhao, Q. Li, L. Liu, Tailored polyimide as positive electrode and polyimide-derived carbon as negative electrode for sodium ion full batteries, Nanoscale 12 (2020) 4729–4735, https://doi.org/10.1039/C9NR09237D.

[51] Y. Wang, P. Bai, B. Li, C. Zhao, Z. Chen, M. Li, H. Su, J. Yang, Y. Xu, Ultralong cycle life organic cathode enabled by ether-based electrolytes for sodium-ion batteries, Adv. Energy Mater. 11 (2021) 2101972, https://doi.org/10.1002/aenm.202101972.

[52] M. Mao, C. Luo, T.P. Pollard, S. Hou, T. Gao, X. Fan, C. Cui, J. Yue, Y. Tong, G. Yang, T. Deng, M. Zhang, J. Ma, L. Suo, O. Borodin, C. Wang, A pyrazine-based polymer for fast-charge batteries, Angew. Chem. Int. Ed. 58 (2019) 17820–17826, https://doi.org/10.1002/anie.201910916.

[53] M. Mohammadiroudbari, K. Qin, C. Luo, Multi-functionalized polymers as organic cathodes for sustainable sodium/potassium-ion batteries, Batteries Supercaps 5 (2022) e202200021, https://doi.org/10.1002/batt.202200021.

[54] R.R. Kapaev, I.S. Zhidkov, E.Z. Kurmaev, K.J. Stevenson, P.A. Troshin, Hexaazatriphenylene-based polymer cathode for fast and stable lithium-, sodium- and potassium-ion batteries, J. Mater. Chem. A 7 (2019) 22596–22603, https://doi.org/10.1039/C9TA06430C.

[55] J. Shi, W. Tang, B. Xiong, F. Gao, Q. Lu, Molecular design and post-synthetic vulcanization on two-dimensional covalent organic framework@rGO hybrids towards high-performance sodium-ion battery cathode, Chem. Eng. J. 453 (2023) 139607, https://doi.org/10.1016/j.cej.2022.139607.

[56] A. Li, Z. Feng, Y. Sun, L. Shang, L. Xu, Porous organic polymer/RGO composite as high performance cathode for half and full sodium ion batteries, J. Power Sources 343 (2017) 424–430, https://doi.org/10.1016/j.jpowsour.2017.01.079.

[57] R.R. Kapaev, A.F. Shestakov, S.G. Vasil'ev, K.J. Stevenson, Conjugated ladder-type polymer with hexaazatriphenylene units as a cathode material for lithium, sodium, and potassium batteries, ACS Appl. Energy Mater. 4 (2021) 10423–10427, https://doi.org/10.1021/acsaem.1c01970.

[58] K. Fan, C. Fu, Y. Chen, C. Zhang, G. Zhang, L. Guan, M. Mao, J. Ma, W. Hu, C. Wang, Framework dimensional control boosting charge storage in conjugated coordination polymers, Adv. Sci. 10 (2023) 2205760, https://doi.org/10.1002/advs.202205760.

[59] M.-S. Wu, P.-C.J. Chiang, High-rate capability of lithium-ion batteries after storing at elevated temperature, Electrochim. Acta 52 (2007) 3719–3725, https://doi.org/10.1016/j.electacta.2006.10.045.

[60] Z. Chen, D.L. Danilov, L.H.J. Raijmakers, K. Chayambuka, M. Jiang, L. Zhou, J. Zhou, R.-A. Eichel, P.H.L. Notten, Overpotential analysis of graphite-based Li-ion batteries seen from a porous electrode modeling perspective, J. Power Sources 509 (2021) 230345, https://doi.org/10.1016/j.jpowsour.2021.230345.

[61] V. Pop, H.J. Bergveld, J.H.G. Op het Veld, P.P.L. Regtien, D. Danilov, P.H.L. Notten, Modeling battery behavior for accurate state-of-charge indication, J. Electrochem. Soc. 153 (2006) A2013, https://doi.org/10.1149/1.2335951.

[62] V. Augustyn, P. Simon, B. Dunn, Pseudocapacitive oxide materials for high-rate electrochemical energy storage, Energy Environ. Sci. 7 (2014) 1597–1614, https://doi.org/10.1039/C3EE44164D.

[63] Y. Shao, M.F. El-Kady, J. Sun, Y. Li, Q. Zhang, M. Zhu, H. Wang, B. Dunn, R.B. Kaner, Design and mechanisms of asymmetric supercapacitors, Chem. Rev. 118 (2018) 9233–9280, https://doi.org/10.1021/acs.chemrev.8b00252.

[64] R.R. Kapaev, A. Zhugayevych, S.V. Ryazantsev, D.A. Aksyonov, D. Novichkov, P.I. Matveev, K.J. Stevenson, Charge storage mechanisms of a π–d conjugated polymer for advanced alkali-ion battery anodes, Chem. Sci. 13 (2022) 8161–8170, https://doi.org/10.1039/D2SC03127B.

[65] X. Kong, J. Zhang, Q. Gong, J. Huang, L. Yin, J. Li, Q. Feng, The Sn–C bond at the interface of a $Sn_2Nb_2O_7$–Super P nanocomposite for enhanced electrochemical performance, New J. Chem. 44 (2020) 4478–4485, https://doi.org/10.1039/C9NJ06281E.